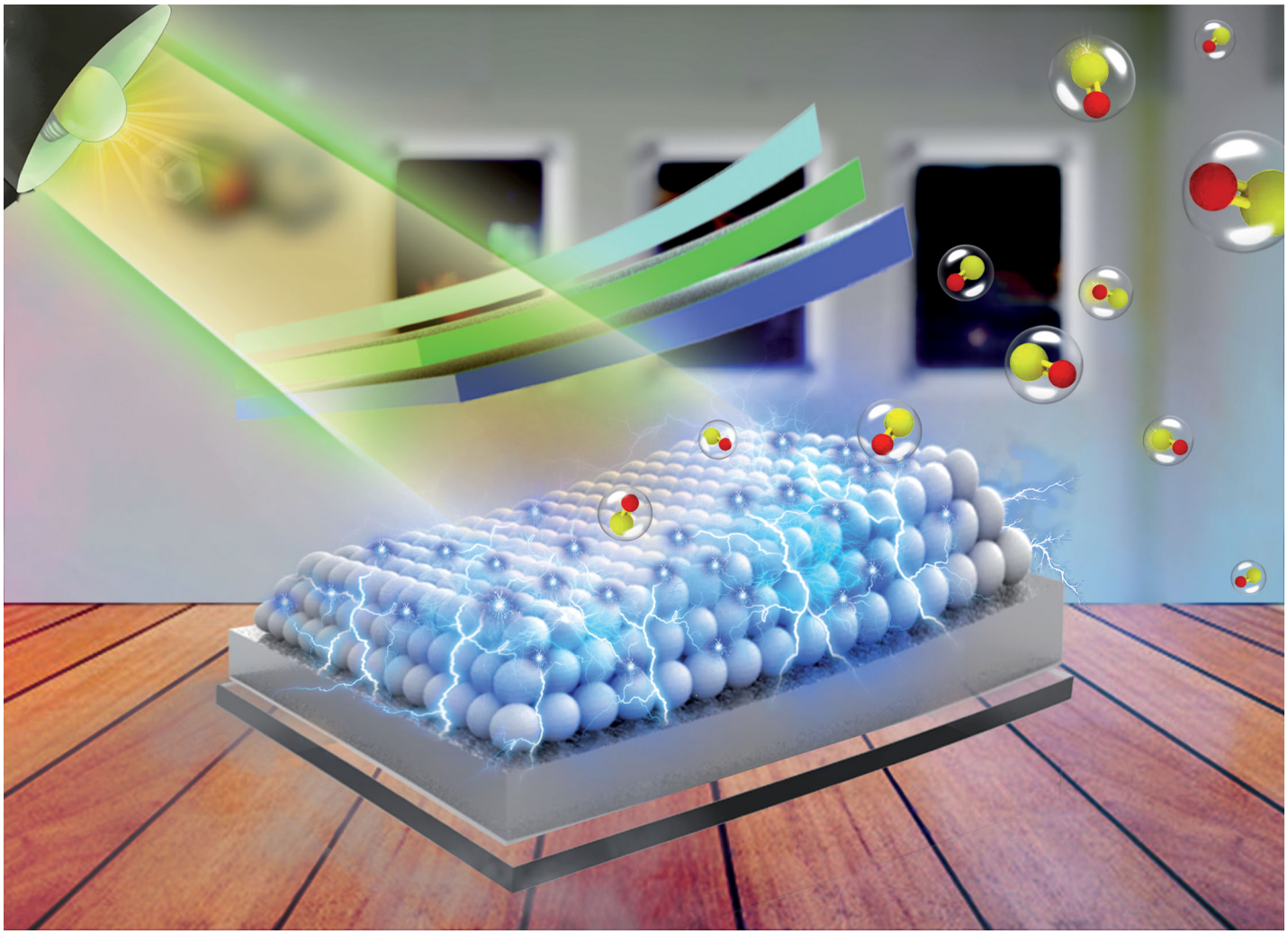

Showcasing research from Prof. Yu-Ching Huang and Prof. Shun-Wei Liu at Ming Chi University of Technology, Taiwan

The effect of ZnO preparation on the performance of inverted polymer solar cells under one sun and indoor light

Various ZnO preparations determine the energy level and carrier recombination behavior of polymer solar cells under 1-Sun and indoor conditions, offering a fundamental insight into future various application designs.

As featured in:

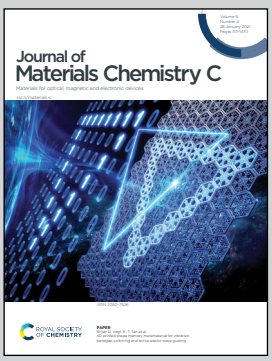

See Yu-Ching Huang, Shun-Wei Liu *et al.*, *J. Mater. Chem. C*, 2021, **9**, 1196.

ROYAL SOCIETY OF CHEMISTRY

rsc.li/materials-c

Registered charity number: 207890

Journal of Materials Chemistry C

ROYAL SOCIETY OF CHEMISTRY

PAPER

View Article Online
View Journal | View Issue

Cite this: J. Mater. Chem. C, 2021, 9, 1196

The effect of ZnO preparation on the performance of inverted polymer solar cells under one sun and indoor light†

Yun-Ming Sung,[a] Abdul Khalik Akbar,[a] Sajal Biring,[a] Chia-Feng Li,[b] Yu-Ching Huang *[b] and Shun-Wei Liu *[a]

In this work, we have investigated in depth the effect of a ZnO layer in between ITO and the active layer of PTB7:$PC_{71}BM$-based polymer solar cells on the device performance under 1 sun and indoor light conditions. Under 1 sun illumination, the PSCs with ZnO nanoparticles show the highest efficiency of 8.33%, which is nearly 14% more compared to the efficiency of the PSCs with ZnO prepared by the sol–gel method due to the shifting of open-circuit voltage (V_{oc}). The PSCs with ZnO nanoparticles show better carrier transport, collection efficiency, reduced bi-molecular recombination, trap-assisted recombination, and charge accumulation as evident from the measurements of light intensity-dependent short circuit current density, V_{oc}, and bulk capacitance of the device. The chemical capacitance extracted from impedance measurements and the trap depth can thoroughly explain the difference in V_{oc}, *i.e.* the shift of energy level and carrier recombination are strongly dependent on the preparation methods of ZnO. Moreover, all the devices show similar performance under indoor light except the PSCs with ZnO prepared by the sol–gel method. The ZnO prepared by the sol–gel method could induce the trap-assisted recombination affecting V_{oc} of the device and resulting in the decrease of its indoor performance. However, we believe that these results might provide a good pathway for the development of polymer solar cells for applications under sunlight and indoor light conditions.

Received 3rd September 2020,
Accepted 6th December 2020

DOI: 10.1039/d0tc04208k

rsc.li/materials-c

1. Introduction

Polymer solar cells (PSCs) are one of the hot research topics in renewable energy due to their advantages of light weight, low cost, good flexibility, and large-area coating scalability. Recently, the power conversion efficiency (PCE) of PSCs has been rapidly improved, thanks to the development of novel non-fullerene acceptors (NFAs). Yuan *et al.* synthesized a novel non-fullerene acceptor of Y6 and the PSC based on PM6:Y6 achieved a PCE of 15.7%.[1] Pan *et al.* further introduced a small amount of $PC_{71}BM$ in PM6:Y6 and improved its performance to 16.7%.[2] In addition to NFA, the development of new donor materials has also effectively improved the PCE of PSCs. Ma *et al.* replaced fluorine in the structure of PM6 with chlorine (PM7) to further reduce the highest occupied molecular orbital (HOMO) of PM6, and thus increased V_{oc} and the PCE of PSCs fabricated from PM7:Y6 to 0.88 V and 17.04%, respectively.[3] Recently, Liu *et al.* synthesized a new donor (D18) enhancing further the PCE of PSCs with the blend of D18 and Y6 to 18.22%.[4] These results reflect the great potential of PSCs for future applications under sunlight. In addition, the study of PSCs to collect energy from indoor light has gradually attracted attention in recent years. The niche market for PSCs could be harvesting indoor energy mainly to power the internet of things (IoT) devices. Unlike outdoor applications, PSCs are supposed to be less damaged by environmental factors such as temperature, humidity and ultraviolet (UV) light and thus PSCs can have a longer operating lifetime in an indoor environment. Besides, indoor light sources exhibit various emission spectrums unlike standard simulated solar cell emission spectrum. Minnaert *et al.* have studied the influence of artificial light sources on the PCE of photovoltaics, and have divided the light sources into three categories. They suggest that the indoor performance of photovoltaics can be measured under one light source from each group instead of under all artificial light sources. For organic photovoltaics, metal halide lamp (HP5) and fluorescent lamp (F7) are the better performing modern light sources.[5] In other cases, PSCs can match well with various indoor light sources because the organic materials have high

[a] Organic Electronics Research Center and Department of Electronic Engineering, Ming Chi University of Technology, New Taipei City 24301, Taiwan. E-mail: swliu@mail.mcut.edu.tw
[b] Department of Materials Engineering, Ming Chi University of Technology, New Taipei City 24301, Taiwan. E-mail: huangyc@mail.mcut.edu.tw

† Electronic supplementary information (ESI) available. See DOI: 10.1039/d0tc04208k

absorption coefficients, an adjustable bandgap and absorption spectrum. Therefore, PSCs exhibit a higher indoor PCE than other types of semiconductor solar cells.[6,7] You *et al.* conducted an in-depth study on the performance optimization of indoor PSCs using various organic materials with different absorption ranges. This study found that the PSC fabricated from PDTBTBz-2F_{anti}:$PC_{71}BM$ exhibits an excellent spectrum matching with indoor light irradiation, especially irradiated by light-emitting diodes (LEDs).[8] The indoor PCEs of the PSCs can be increased to 23.1% (LED, 1000 l×), which is better than those of the crystallized silicon solar cells. In addition, Freunek *et al.* calculated the maximum theoretical value of indoor PCE based on the Schockley–Queisser limit under various indoor light sources, which can reach 72% with an organic material with an energy bandgap of 2.1 eV under the light source of sodium discharge lamp. These high experimental and theoretical indoor PCEs show the huge potential application of PSCs towards harvesting indoor energy in the future.[9]

In addition to donor and acceptor materials, the carrier transport layer also plays a very important role in the PCE and stability of PSCs. Considering the stability of PSCs, the inverted PSCs, which utilize a high work-function metal as the anode and the metal oxide covering the transparent conductive electrode, indium tin oxide (ITO), as an electron transport layer (ETL), have become the mainstream structure of the PSCs. Many metal oxides have been developed for the ETLs of inverted PSCs including TiO_2, SnO_2, and ZnO. These metal oxides can be easily modified by using dopants,[10–16] surface modifiers[17–21] and self-assembled monolayers[22–24] to improve the chemical and physical properties, such as electrical conductivity, work function and surface energy, thereby improving the PCE of PSCs. Among these various metal oxides, ZnO is the most conventional ETL due to the advantages of low toxicity, easy preparation, low annealing temperature, high mobility, high chemical stability, and the possibility of the solution process. However, most studies have discussed the effect of ZnO on the PCEs of PSCs under 1 sun illumination, whereas the research related to the indoor PCE is still lacking.

In this study, we have explored the effects of ZnO prepared by different processes as ETLs of the PSC on device efficiency under 1 sun and indoor light conditions. The ZnO nanoparticles (ZnO NPs) and ZnO prepared by the sol–gel method with various annealing times (20, 30 and 60 min), which are named NZ, SZ-20, SZ-30 and SZ-60, respectively, were used as the ETLs of PSCs. These ETLs fabricated from various ZnO exhibit different surface morphology, internal defects, and crystallinity. The surface morphology and shape formation of ZnO can be controlled by the crystal growth using different annealing treatment, solvent selectivity and the solution concentrations.[25–28] The surface morphology of the SZ films prepared in this study is more like the cluster structure, which has been characterized in our previous research.[29] Under 1 sun illumination, the PSCs fabricated from SZ-20, SZ-30 and SZ-60 show similar PCEs of 7.14%, 7.11% and 7.18%, respectively, which is comparable to the value reported by other studies in the literature.[30,31] On the other hand, the PSC fabricated from NZ shows a higher PCE of 8.33% with better open circuit voltage (V_{oc}), short circuit current density (J_{sc}), and fill factor (FF) leading to 14% enhancement in PCE compared with that of the PSC based on ZnO prepared by the sol–gel method. By measuring the J_{sc} and capacitance–voltage behaviors under various light intensities, we infer that the PSCs fabricated from NZ have better carrier transport and collection efficiency, and also exhibit the lowest charge accumulation at the interface between ZnO NPs and the active layer. Besides, the NZ-based PSCs show the lowest trap-assisted recombination and ZnO trap depth in comparison with the SZ-based PSCs. These results can well explain the efficiency changes for PSCs fabricated from different ZnO ETLs under 1 sun illumination. Interestingly, the indoor PCEs of the PSCs with various ETLs are not much different. The indoor PCEs of PSCs with NZ, SZ-20, SZ-30 and SZ-60 under indoor light illumination (TL84, 1000 lx) are 14.38%, 13.53%, 14.28% and 14.70%, respectively, and are also comparable to the values reported in the literature.[32] The devices show similar values of occupied electron density of states (DOS) estimated from measuring the chemical capacitance under the indoor light condition. The similar DOS values of the devices indicate the comparable carrier recombination in these devices with different ETLs. In addition, the trap-assisted recombination of the PSCs under indoor light is greatly increased compared to that of PSCs under 1 sun, especially for the devices with SZ-20 ETL. Therefore, we can speculate that the trap-assisted recombination behavior dominates the PCE of PSCs under indoor light conditions. Our study on the PCEs of PSCs under 1 sun and indoor light conditions provides a clear insight to achieve a high indoor PCE of PSCs.

2. Experiment

2.1. Materials

Zinc acetate di-hydrate ($Zn(CH_3COO)_2{\cdot}2H_2O$, 99%), 2-methoxyethanol ($CH_3OCH_2CH_2OH$, 99.8%), ethanolamine ($NH_2CH_2CH_2OH$, 99.5%), ethanol (C_2H_5OH, 99.8%), chlorobenzene (C_6H_5Cl, 99.8%), 1,8-diiodooctane ($C_8H_{16}I_2$, 98%), and molybdenum(VI) oxide (MoO_3, 99.5%) were purchased from Sigma Aldrich. Lithium hydroxide monohydrate ($LiOH{\cdot}H_2O$, 56%) was purchased from Acros Organics. PTB7 was purchased from 1-Material and $PC_{71}BM$ was purchased from Solenne B. V. The 15 $\Omega\ \square^{-1}$ ITO was purchased from Lumtec Corporation.

2.2. Solution preparation

The sol–gel ZnO was prepared by dissolving 1.1 g of zinc acetate dihydrate and 0.31 g of ethanolamine in 10 mL of 2-methoxyethanol and then stirring for 8 hours. ZnO nanoparticles were synthesized by the chemical precipitation method reported by Wang *et al.*[33] First, 4.4 g of zinc acetate di-hydrate was dissolved in 220 mL of ethanol and then stirred at 700 rpm for 5 min. Then, 1.1 g of lithium hydroxide monohydrate and 4 mL of DI water were added to the previous solution followed by vigorous stirring. After the color of the solution changed to transparent, the solution was put in a water bath at 60 °C and stirred at 700 rpm for 30 min. The reacted solution was then centrifuged at 3000 rpm for 3 min and then the suspension

was removed. The resulting ZnO white powder was re-dispersed in IPA at a concentration of 10 mg mL^{-1} with 0.15% ethanolamine as the dispersant. The solution of PTB7:$PC_{71}BM$ was prepared by dissolving PTB7 and $PC_{71}BM$ (1 : 1.5, 25 mg mL^{-1}) in chlorobenzene with 3% 1,8-diiodooctane as the additive.

2.3. Device fabrication

The patterned ITO glasses were cleaned by DI Water, acetone and IPA in an ultrasonic bath and then dried using flowing nitrogen gas. The ZnO film used in this study was prepared by the sol–gel ZnO method or ZnO nanoparticles. The ZnO films prepared using sol–gel ZnO were fabricated by spin coating the sol–gel ZnO precursor on cleaned ITO glasses at 3000 rpm for 30 s and then annealing at 170 °C for 20 min, 30 min and 60 min, respectively. The ZnO film prepared using ZnO nanoparticles was fabricated by the same method as the sol–gel ZnO except with thermal annealing. After ZnO film deposition, the PTB7:$PC_{71}BM$ solution was coated on ZnO film at 2000 rpm for 30 s and then dried in a vacuum chamber. Then, 5 nm MoO_3 and 100 nm Ag were deposited on the PTB7:$PC_{71}BM$ layer by thermal evaporation under 2×10^{-6} torr. The resulting device area is 0.04 cm^2.

2.4. Device characteristics

The device performance under sunlight conditions was measured using a 3A class AM 1.5G solar simulator (SS-X100R, Enlitech). The sunlight intensity can be tuned from 0.01 to 1 sun by adjusting the mechanical iris aperture in the simulator without changing the spectrum. The external quantum efficiency (EQE) was measured by solar cell spectral response measurement (QE-R3011, Enlitech). The device performance under indoor light was measured using an integrated system (from Industrial Technology Research Institute, ITRI) composed of a power meter (Keithley 2401) and a light source of Philips TLD 18W/830. The intensity of indoor light can be modulated to 200, 400, 600, 800 and 1000 l×, which correspond to 0.058, 0.116, 0.174, 0.223 and 0.290 mW cm^{-2}, respectively. The transmittance and reflectance for various ZnO films were measured by UV-visible spectroscopy (V-770, Jasco) using a glass substrate. The photoluminescence (PL) measurements were conducted using a FluroMax Spectrofluorometer (FluoroMax Plus, HORIBA Jobin Yvon) using an ozone-free xenon arc lamp with the excitation source of 305 nm. The X-ray diffraction (XRD) was done using a high-power X-ray diffractometer (Rigaku TTRAX 3) with Cu K_α radiation. The Fourier transform infrared (FTIR) spectra were obtained by Fourier transform infrared spectroscopy (Spectrum 100, PerkinElmer). The ZnO film topography was measured by a desktop AFM instrument (Innova, BRUKER). The impedance measurements were conducted by electrochemical impedance measurement (Material Lab XM module). The capacitance–voltage measurements were carried out from 0 to 1.5 V with the frequency and ac voltage of 1 kHz and 50 mV, respectively. The Nyquist plot was measured from 1 MHz to 1 Hz at an applied voltage set to the open circuit voltage of the device. The temperature-dependent measurements were conducted using an LED light source (LSH 73320, Newport) and a cooling system equipped with liquid nitrogen, a cryogenic tube (Janis VPF-100) and a temperature controller (Lake Shore 335).

3. Results and discussion

Fig. 1 shows the energy level alignment, device structure, current–voltage (J–V) curves, and EQE of the inverted PSCs based on PTB7:$PC_{71}BM$, and Table 1 summarizes the detailed photovoltaic characteristics under 1 sun illumination. In this study, various ZnO layers were used as the ETLs of PSCs including ZnO NPs (NZ) and sol–gel ZnO annealed for 20, 30 and 60 min (SZ-20, SZ-30 and SZ-60). Under 1 sun illumination, the PSCs fabricated with SZ-20, SZ-30 and SZ-60 show the efficiencies of 7.14%, 7.11% and 7.18%, respectively. However, the PSCs fabricated from the NZ show a higher PCE of 8.33% with improved V_{oc}, J_{sc} and FF. The EQEs shown in Fig. 1d reveal a similar spectrum response in these devices from 450 to 700 nm.

However, the EQE difference from 300 to 450 nm can be attributed to the difference in transmittance and reflectance of the various ZnO films, and the results are shown in Fig. S1 (ESI†). The NZ film shows the highest transmittance and the lowest reflectivity, resulting in a higher EQE for NZ-based devices in the 300–400 nm region. The topographies of these ZnO films are shown in Fig. S2 (ESI†) using AFM. Fig. S2a (ESI†) shows the topography of the film prepared with NZ revealing the smoothest surface with a root-mean-square (rms) surface roughness of 1.66 nm. The topographies of the films prepared by SZ-20, SZ-30 and SZ-60 show similar rms surface roughness of 2.66, 2.53, and 2.65 nm, respectively. The smoother ZnO surface may improve the interfacial contact between ETL and active layer, and then enhance the electron transport for the NZ-based PSCs. However, Richardson *et al.*[34] have reported that the PCE of the PSC based on PTB7:$PC_{71}BM$ is not sensitive to the surface roughness of the ZnO film, even though the rms

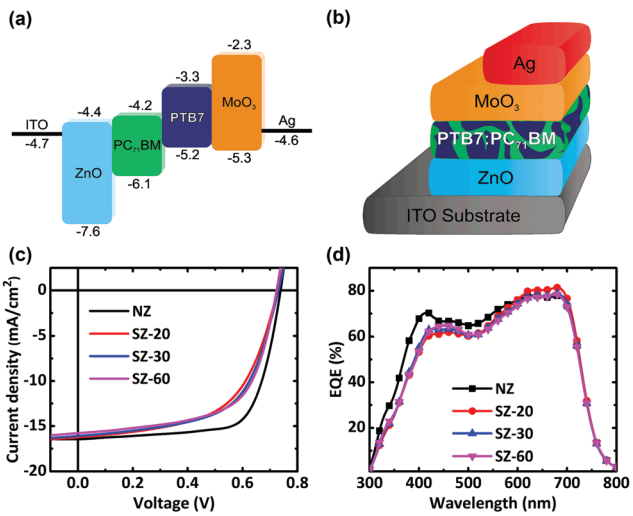

Fig. 1 (a) The energy level alignment, (b) device structure, (c) current density–voltage curves under 1 sun condition and (d) EQE spectra of the inverted PTB7:$PC_{71}BM$-based PSCs.

Table 1 A summary of device electrical characteristics with different ZnO preparation under 1 sun conditions. The values in brackets are average values from 10 devices

ETL	J_{sc} (mA cm^{-2})	V_{oc} (V)	FF (%)	η (%)
NZ	16.54 (16.35 ± 0.04)	0.75 (0.75 ± 0.002)	67.11 (66.84 ± 0.46)	8.32 (8.22 ± 0.07)
SZ-20	16.24 (16.02 ± 0.05)	0.72 (0.72 ± 0.002)	60.49 (58.47 ± 0.51)	7.07 (6.79 ± 0.06)
SZ-30	16.09 (16.11 ± 0.11)	0.73 (0.73 ± 0.003)	59.82 (58.68 ± 0.50)	7.04 (6.90 ± 0.06)
SZ-60	15.78 (16.17 ± 0.10)	0.73 (0.73 ± 0.002)	62.18 (59.46 ± 0.46)	7.16 (7.03 ± 0.04)

surface roughness of the ZnO layer changes from 3 to 13.3 nm. Therefore, the small difference in the rms surface roughness of these ZnO layers might not be the main reason for the improved PCEs of the PSCs fabricated from NZ.

To further investigate the reasons behind the change in PCE, we measured the J_{sc} and V_{oc} of the devices under different light intensities, which can be used to analyze the mono- or bi-molecular carrier recombination behaviors.[35–37] Fig. 2a shows the J_{sc} obtained under various sunlight intensities. The relation between the J_{sc} and light intensity is given by $J_{sc} \propto I^{\alpha}$, where I is the light intensity, and $\alpha = 1$ means that carriers are transported to their corresponding electrodes without recombination. The α values of the PSCs fabricated from SZ-20, SZ-30, and SZ-60 were 0.912, 0.920 and 0.915, respectively. In the case of the PSCs with NZ, the α value slightly improves to 0.932, which means that the PSCs with NZ exhibit a better carrier transport and carrier collection efficiency under 1 sun conditions. Fig. S3 (ESI†) shows the carrier mobility extracted from the impedance measurements. The results indicate that the carrier mobility in the PSCs with NZ is higher than that of the PSCs with SZ, and all the PSCs fabricated from SZ have similar carrier mobility irrespective of the annealing time for the SZ layers. The mobility in these PSCs is consistent with the results shown in Fig. 2a. The enhanced mobility in the NZ-based PSCs could be attributed to the good crystallinity of the ZnO NPs. Fig. 2b shows the measured V_{oc} at various sunlight intensities. Under open-circuit conditions, all carriers can be assumed to be recombined, and the recombination behavior can be expressed by the equation of $V_{oc} \propto nkT/q \ln I$, where n is the slope of V_{oc} *vs.* light intensity curve, k is the Boltzmann constant, T is the temperature and q is the elementary charge. The PSCs fabricated with SZ-20, SZ-30, SZ-60 and NZ show slopes of 1.778, 1.596, 1.525, and 1.368, respectively. The slope closer to 1 means that less trap-assisted recombination happens in the device. Therefore, we can infer that PSCs fabricated from NZ have the lowest trap states and lead to the lowest carrier recombination under 1 sun conditions. Besides, the slopes of the SZ-based PSCs decrease as the annealing time increases, which means that the traps and trap-assisted recombination in the SZ films can be reduced with prolonged annealing time. We also characterized the energy transfer in the NZ and SZ films by measuring PL and energy trap depth. Fig. S4 (ESI†) shows the emission peaks of 367, 377, 375 and 373 nm for the films deposited from ZnO NPs, SZ-20, SZ-30 and SZ-60, respectively. The red shift of the emission peak indicates that there is a trap state in the ZnO films.[38] Therefore, the NZ film shows a wider bandgap and lower trap state compared to the SZ films. Besides, Fig. S5 (ESI†) shows the J_{sc} obtained at various

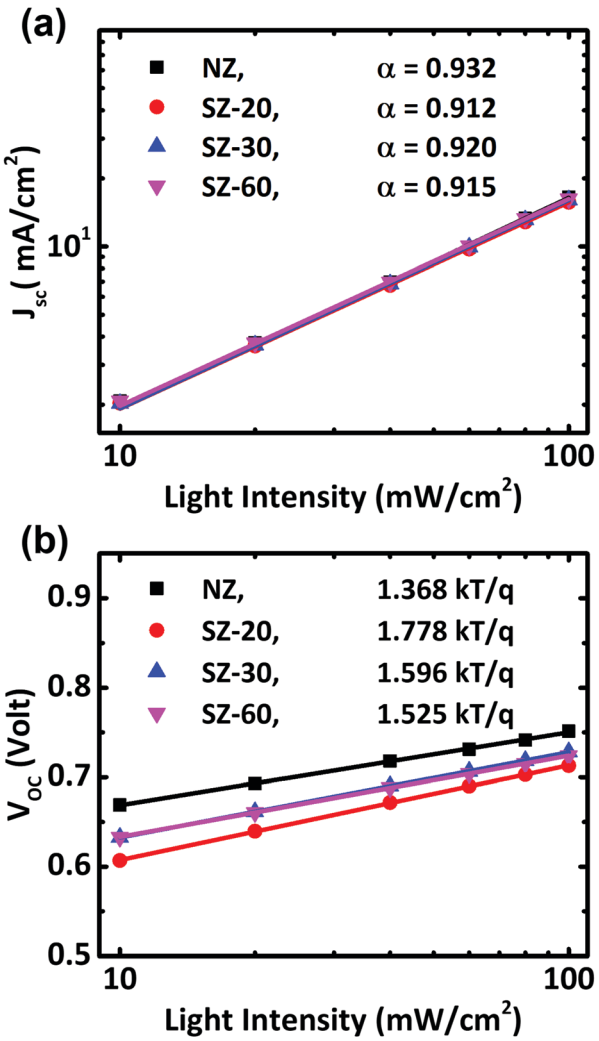

Fig. 2 (a) Bimolecular and (b) monomolecular recombination of various devices under sunlight conditions.

temperatures, and the trap depth of devices can be extracted from the formula of $J_{sc} = J_0 \exp(-\Delta/kT)$, where Δ is the trap depth. The values of trap depth of the PSCs fabricated from NZ, SZ-20, SZ-30, and SZ-60 are 15.8, 21.6, 24.8 and 23.7 meV, respectively. The deeper trap depth in SZ-based PSCs can be attributed to the lower crystallinity of sol–gel ZnO and the defects in the ZnO layer would become a recombination center resulting in the recombination of electrons in ZnO with holes in PTB7.[39,40]

The XRD results shown in Fig. 3a also reveal the difference in crystallinity of ZnO prepared by different methods. Among

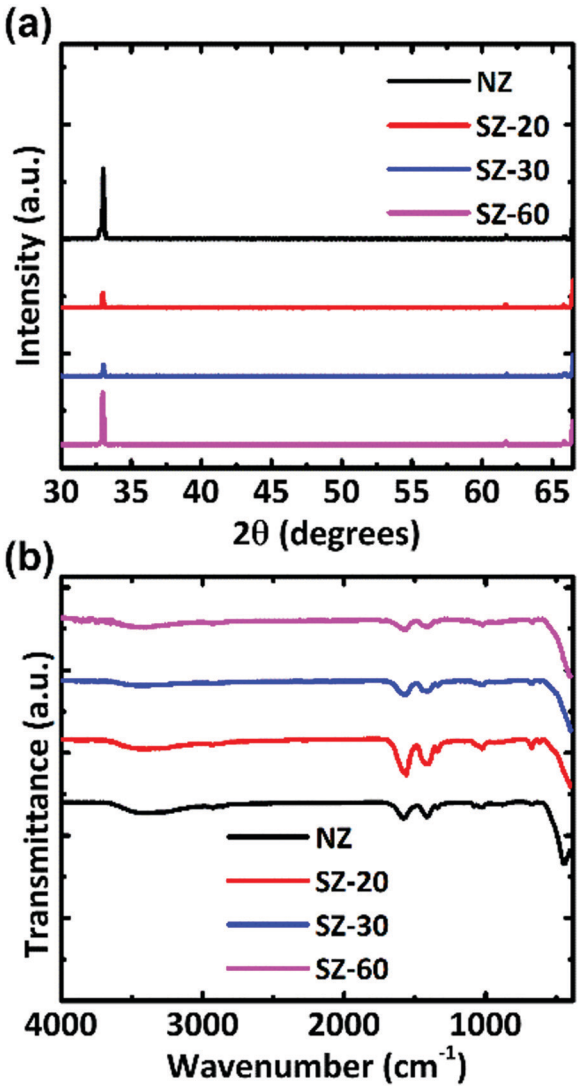

Fig. 3 (a) XRD patterns and (b) FTIR spectra of different ZnO films. All data are normalized to film thickness.

the SZ films, SZ-20 exhibits the lowest crystallinity because of the short annealing time. With the increasing annealing time, the crystallinity of the SZ film is improved and the SZ-60 shows the highest crystallinity. Interestingly, the NZ film shows the highest crystallinity even without additional thermal annealing. The highest crystallinity of the NZ film can be attributed to the good crystal formation during the synthesis process, because the zinc acetate dihydrate has been completely forming the ZnO through a chemical reaction. Fig. 3b shows the FTIR spectra of the various ZnO films. The absorption peak at 508 cm^{-1} indicates the Zn–O bond, and the increasing intensity of the Zn–O bond implies that more Zn can be oxidized to ZnO. The NZ film exhibits the strongest Zn–O absorption, and the absorption intensity of Zn–O increased with the annealing time on the SZ film, which is consistent with the XRD results. The broad band from 3000 to 3500 cm^{-1} can be ascribed to the stretching mode of the O–H bond. In addition, the absorption from 1000 to 2000 cm^{-1} resulted from the remaining ethanolamine, and its intensity decreased with the increasing annealing time.[47] This result points out that the subsequent thermal annealing process can remove the ethanolamine residues.

Charge accumulation at the interface between the active layer and the ZnO film is also an important issue in PSCs. To analyze the extent of charge accumulation, we measured the device capacitance at various applied voltages, and the results are shown in Fig. 4. The diagram of capacitance–voltage (C–V) can be divided into three parts: (1) during the applied voltage sweep from zero to positive, the photo-generated carriers begin to accumulate in the device due to the energy barrier at the interface between the active layer and ZnO film. (2) At the V_{peak}, the capacitance becomes maximum due to the balance of injected carrier and photo-generated carrier. (3) When the applied voltage exceeds V_{peak}, the injected carriers become dominant and then recombine with the photo-generated carriers leading to a reduction in capacitance. Furthermore, changing the light intensity would affect the V_{peak} value due to the different extents of photo-generated carrier accumulation.[41–43] Fig. 4 shows the C–V measurement of the NZ- and SZ-based PSCs at a sunlight intensity from 10 to 100 mW cm^{-2}. The values of V_{peak} at 10 mW cm^{-2} light illumination are 0.66, 0.63, 0.65 and 0.68 V for the devices fabricated from NZ, SZ-20, SZ-30 and SZ-60, respectively. Under 100 mW cm^{-2} light illumination, the shifts of V_{peak} are 0.088, 0.166, 0.180 and 0.177 V for the PSCs fabricated from NZ, SZ-20, SZ-30 and SZ-60, respectively. The shift of V_{peak} to a lower value can be attributed to the higher charge accumulation at the interface between ZnO and the active layer.[44] Therefore, the PSCs fabricated from NZ show the lowest extent of charge accumulation, which can be attributed to the higher carrier mobility and lower trap depth as discussed in previous results. Additionally, all the SZ-based PSCs show similar charge accumulation having good agreement with the carrier mobility and trap depth. Fig. S6 (ESI†) shows the carrier mobility

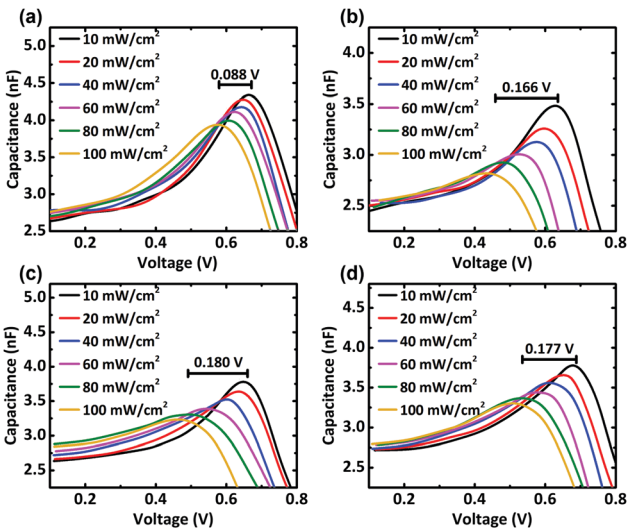

Fig. 4 The results of C–V measurement measured at room temperature and various light intensities for the PSCs fabricated from (a) NZ, (b) SZ-20, (c) SZ-30, and (d) SZ-60.

under various temperatures. The mobility difference in SZ-based PSCs at high and low temperatures is much higher than that of NZ-based PSCs, indicating the higher barrier of adjacent hopping state in SZ-based PSCs. Besides, the activation energies of the PSCs fabricated from NZ, SZ-20, SZ-30 and SZ-60 are 154, 201, 187, and 181 meV, respectively.[45] Both the temperature-dependent mobility and activation energy indicate that the SZ-based PSCs exhibit high energy disorder. Therefore, we can conclude that the difference in the PCE of PSCs fabricated from different ZnO under 1 sun illumination can be attributed to the difference in carrier mobility and trap depth leading to the charge accumulation at the interface of ZnO and the active layer.

Chemical capacitance is another important characteristic in PSCs, which is formed by the excess charges and can be used to analyze the change in the electron occupancy of acceptor DOS and carrier recombination. The relationship between the chemical capacitance and DOS can be expressed as $C_\mu = q^2 L g_n(V_F)$, where C_μ is the chemical capacitance, L is the thickness of the active layer, and g_n is the occupied DOS. According to the literature report published by Garcia-Belmonte *et al.*,[46] the shift of C_μ can be used to analyze the effective energy level change (ΔV_e), and the ΔV_e can be represented by $\Delta V_e = \Delta E_{LUMO,acceptor} - \Delta E_{HOMO,donor}$. In this study, we used various ZnO as ETLs of the PSCs, and the different ZnO layers would change the energy level alignment at the interface of ZnO/$PC_{71}BM$ and then change the effective acceptor LUMO. Therefore, we have studied the change in chemical capacitance of the PSCs at open circuit condition, and the results are shown in Fig. 5. Fig. 5a shows the chemical capacitance–voltage graphs extracted from the impedance measurements. The straight lines represent the occupied DOS behavior, which can be used to analyze the shift of the effective energy level (ΔV_e). Considering the PSCs fabricated from ZnO NPs as the reference, the relative changes of V_{oc}, trap depth and V_e of the SZ-based PSCs can be calculated. Table 2 summarizes the experimental V_{oc}, ΔV_{oc}, Δ(trap depth), ΔV_e and calculated ΔV_{oc} (noted as ΔV_{oc}^*) of the PSCs. If we assume the trap depth is the energy loss of carrier recombination, then the ΔV_{oc}^* can be calculated by $\Delta V_{oc}^* = \Delta V_e + \Delta(\text{trap depth})$. The ΔV_{oc}^* shows a comparable value to ΔV_{oc}, which insinuates that the V_{oc} change in PSCs can be attributed to the shift of energy level and carrier recombination. The chemical capacitance–light intensity plots shown in Fig. 5b imply that the gap between the chemical capacitance of PSCs fabricated from various ZnO layers would be reduced as the light intensity decreases. Therefore, we can speculate that the NZ- and SZ-based PSCs have similar occupied DOS under indoor light due to the low light intensity, which means that the carrier recombination behaviors of these devices may be very similar. The indoor DOS behavior will be presented later.

The foregoing discussion was about the effect of different ZnO as ETLs on the PCEs of PSCs under 1 sun conditions. Now, we will discuss the PCEs of the PSCs fabricated from NZ and SZ under indoor light illumination (light source is TL84). The *J*–*V* curves obtained at 1000 l× indoor light illumination are shown

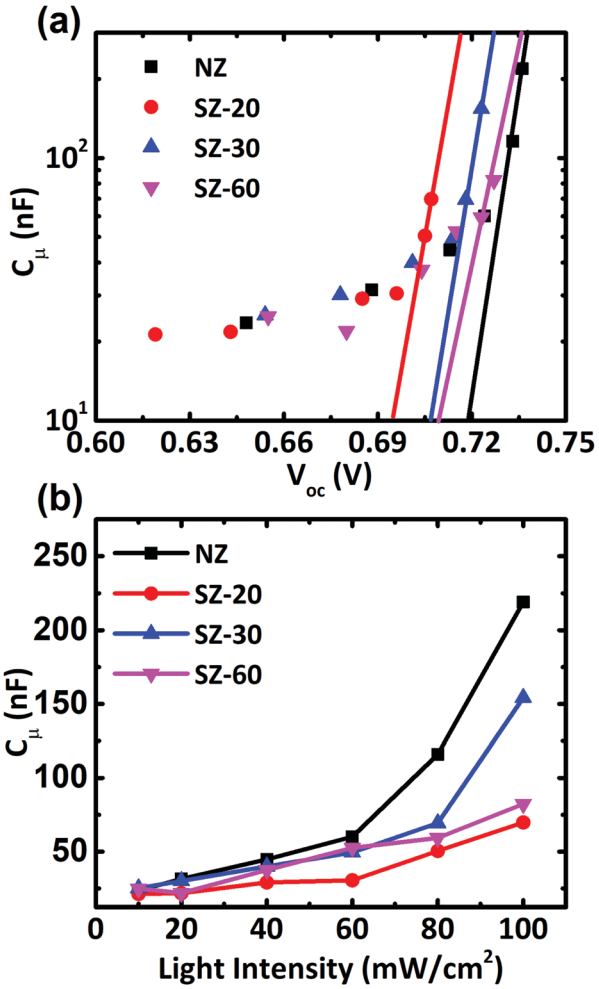

Fig. 5 The results of chemical capacitance extracted from impedance measurements under open circuit conditions. The value of C_μ are the same in (a) C_μ–V_{oc} and (b) C_μ–light intensity but in different presented format.

Table 2 A summary of the change of V_{oc}, trap depth and energy level, while the ZnO NP-prepared PSCs are set as the reference. The ΔV_{oc} is extracted from the device's *J*–*V* curve. Δtrap depth and ΔV_e are extracts from the temperature-dependent J_{sc} measurement and C_μ–V_{oc} diagram, respectively. ΔV_{oc}^* are calculated by ΔV_{oc}^* = Δtrap depth + ΔV_e

ETL	V_{oc} (V)	ΔV_{oc} (mV)	Δtrap depth (mV)	ΔV_e (mV)	ΔV_{oc}^* (mV)
NZ	0.75	—	—	—	—
SZ-20	0.72	−30	−5.8	−24.0	−29.8
SZ-30	0.73	−20	−9.0	−11.9	−20.9
SZ-60	0.73	−20	−7.9	−9.3	−17.2

in Fig. S7 (ESI†), and the photovoltaic characteristics are summarized in Table 3. In addition, the detailed performance of the PSCs illuminated under various indoor light intensities are listed in Table S1 (ESI†). PSCs fabricated from SZ-20, SZ-30, and SZ-60 exhibit PCEs of 13.53%, 14.28% and 14.7%, respectively. It is worth noting that the PCE of NZ-based PSCs is 14.38%, which is comparable to those of SZ-based PSCs. Unlike the PCE obtained at 1 sun illumination, the PCEs of NZ-based

Table 3 The summary of ZnO NP- and ZnO sol–gel-prepared PSCs' electrical characteristics under a light intensity of 0.290 W cm^{-2} (1000 lux) from a light source of Philips TLD 18W/830. The values in brackets are average values from 10 devices

ETL	J_{sc} (μA cm^{-2})	V_{oc} (V)	FF (%)	η (%)
NZ	112.11 (112.57 ± 0.47)	0.58 (0.58 ± 0.002)	64.57 (62.64 ± 0.42)	14.48 (14.20 ± 0.08)
SZ-20	111.66 (111.56 ± 0.21)	0.54 (0.54 ± 0.001)	64.83 (63.64 ± 0.27)	13.53 (13.15 ± 0.07)
SZ-30	116.89 (115.86 ± 0.43)	0.57 (0.57 ± 0.002)	61.71 (60.64 ± 0.28)	14.28 (13.83 ± 0.06)
SZ-60	118.59 (116.02 ± 0.53)	0.57 (0.57 ± 0.004)	63.11 (63.12 ± 0.48)	14.7 (14.41 ± 0.06)

PSCs do not exhibit a better indoor PCE than those of the SZ-based PSCs. The main difference in the characteristics of PSCs is V_{oc}, which is 0.58, 0.54, 0.57, and 0.57 V for the PSCs prepared with NZ, SZ-20, SZ-30, and SZ-60, respectively. Likewise, we measured the J_{sc} and V_{oc} at various indoor light intensities to analyze the recombination behavior in these PSCs, and the results are shown in Fig. 6a and b. Interestingly, all α values under indoor light conditions are higher than those under 1 sun conditions. The reason for the increasing α value can be attributed to the lower carrier concentration under indoor light, which leads to lower bi-molecular recombination. The α values of the PSCs fabricated from NZ, SZ-20, SZ-30, and SZ-60 are 0.995, 0.946, 0.965 and 0.966, respectively. As mentioned earlier, the improved α values of NZ-based PSCs imply better carrier transport and collection efficiency. However, the tendency of the α values is not entirely related to the change in the indoor PCE of PSCs. The relationship between light intensity and V_{oc} is plotted in Fig. 6b, and the slopes of a linear fit to these data give n equal to 1.441, 2.031 1.698, and 1.698 for the PSCs fabricated from NZ, SZ-20, SZ-30, and SZ-60, respectively. Interestingly, the n value of the PSCs fabricated from SZ-20 largely increased from 1.778 to 2.017 when the illuminated light switched from 1 sun to indoor light. The larger n value under indoor condition suggests that the devices suffer from severe trap-assisted recombination. We speculate that the increased trap-assisted recombination can be attributed to the lower internal field at low light intensity. This result also reveals that the PSCs illuminated by a higher light intensity will increase the internal field in the PSCs, and the high internal field can prevent the carriers from transporting back to recombination. The low internal field generated under low light intensity cannot hinder the backward transport of carriers. Therefore, the lowest indoor PCE of the PSCs fabricated from SZ-20 is due to the higher trap-assisted recombination. Furthermore, the chemical capacitance under indoor light shown in Fig. 6c indicates that the energy shifts become smaller for the devices fabricated from SZ-30 and SZ-60, which lead to the similar efficiency with NZ-based devices under indoor conditions. In contrast, SZ-20 has a significant shift in effective energy level as shown in Table 4, which means that the carrier recombination behavior of SZ-20 deteriorates under indoor conditions. Fig. 6d shows the trap depth under indoor light, where the trap depths of the devices fabricated from NZ, SZ-20, SZ-30 and SZ-60 are 8.49, 17.40, 13.90, and 12.67 meV, respectively. The trap depth under indoor conditions is consistent with that under 1 sun conditions.

Table 4 A summary of the change in V_{oc}, trap depth and energy level, while the ZnO NP-prepared PSCs are set as the reference under indoor light conditions

ETL	V_{oc} (V)	ΔV_{oc} (mV)	Δtrap depth (mV)	ΔV_e (mV)	ΔV_{oc}^* (mV)
NZ	0.58	—	—	—	—
SZ-20	0.54	−40	−8.9	−31.7	−40.6
SZ-30	0.57	−10	−5.4	−9.1	−14.5
SZ-60	0.57	−10	−4.2	−6.9	−11.1

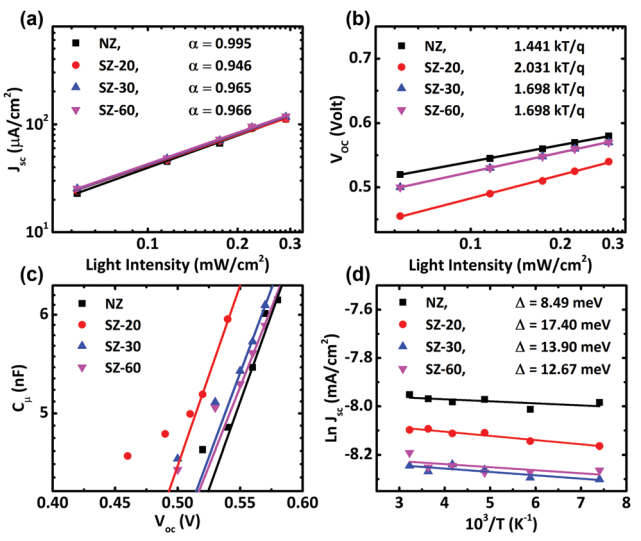

Fig. 6 (a) The bimolecular, and (b) monomolecular recombination and (c) chemical capacitance under indoor light. (d) The trap depth under 1000 lux intensity of indoor light was acquired to calculate the effective energy shift.

4. Conclusions

In this research, we have studied the effect of ZnO thin films prepared by different methods on the performance of PSCs under one sun and indoor light conditions. The J_{sc} and V_{oc} under various one-sun light intensities indicate that the PSC prepared with ZnO NPs has better carrier transport, carrier collection efficiency, reduced bi-molecular recombination and trap-assisted recombination. Besides, the PSC with ZnO NPs has the lowest carrier accumulation at the interface of the active layer and ZnO film, by using the C–V measurements under various light intensities. The V_{oc} difference of the PSC is quite consistent with the energy level shift extracted from chemical capacitance and trap depth of PSC, which indicates that the V_{oc} difference can be attributed to the energy level shift of the

effective LUMO of the acceptor material and the energy loss from carrier recombination. Therefore, the factors including carrier transport, and bi-molecular and trap-assisted recombination are important for the performance of PSC under 1 sun conditions. As for the indoor light condition, all the PSCs show comparable efficiency except for the device fabricated from SZ-20. Compared to the 1 sun condition, the J_{sc} of the devices under various indoor light intensities indicates improved carrier transport, collection efficiency, and reduced bi-molecular recombination, which can be attributed to the lower carrier concentration under indoor light conditions. In addition, the PSCs fabricated from NZ, SZ-30 and SZ-60 show comparable chemical capacitance indicating similar recombination behavior under low light intensity. The V_{oc} under various indoor light intensities indicates higher trap-assisted recombination compared to the 1 sun condition, especially for the PSC with SZ-20. The higher trap-assisted recombination can be attributed to the lower internal field due to the low light intensity. Therefore, the trap-assisted recombination becomes dominant for the PSC under indoor light conditions. We can conclude that higher ZnO crystallinity can improve charge mobility, and then improve PCEs of PSCs under 1 sun and indoor light conditions. In addition, reducing surface traps can inhibit trap-assisted recombination, which plays a crucial role in PCEs of PSCs under indoor light conditions. We believe the in-depth investigation carried out in this study can provide a good strategy to develop an efficient PSC for successful applications under sunlight and indoor light.

Conflicts of interest

There are no conflicts to declare.

Acknowledgements

The authors acknowledge financial support from the Ministry of Science and Technology (Grant No. MOST 107-2218-E-131-007-MY3, 108-2221-E-131-027-MY2 and 109-2223-E-131-001-MY3), Academia Sinica (AS-SS-109-05). The corresponding author (S.-W. Liu) is grateful to Mr H.-H. Wu, Syskey Technology Co., Ltd (Taiwan), for his assistance in designing the fabrication system.

References

1 J. Yuan, Y. Zhang, L. Zhou, G. Zhang, H. L. Yip, T. K. Lau, X. Lu, C. Zhu, H. Peng, P. A. Johnson, M. Leclerc, Y. Cao, J. Ulanski, Y. Li and Y. Zou, *Joule*, 2019, **3**, 1140–1151.
2 M. A. Pan, T. K. Lau, Y. Tang, Y. C. Wu, T. Liu, K. Li, M. C. Chen, X. Lu, W. Ma and C. Zhan, *J. Mater. Chem. A*, 2019, **7**, 20713–20722.
3 R. Ma, T. Liu, Z. Luo, Q. Guo, Y. Xiao, Y. Chen, X. Li, S. Luo, X. Lu, M. Zhang, Y. Li and H. Yan, *Sci. China: Chem.*, 2020, **3**, 6–11.
4 Q. Liu, Y. Jiang, K. Jin, J. Qin, J. Xu, W. Li, J. Xiong, J. Liu, Z. Xiao, K. Sun, S. Yang, X. Zhang and L. Ding, *Sci. Bull.*, 2020, **65**, 272–275.
5 B. Minnaert and P. Veelaert, *Energies*, 2014, **7**, 1500–1516.
6 H. S. Ryu, S. Y. Park, T. H. Lee, J. Y. Kim and H. Y. Woo, *Nanoscale*, 2020, **12**, 5792–5804.
7 C. L. Cutting, M. Bag and D. Venkataraman, *J. Mater. Chem. C*, 2016, **4**, 10367–10370.
8 Y. J. You, C. E. Song, Q. V. Hoang, Y. Kang, J. S. Goo, D. H. Ko, J. J. Lee, W. S. Shin and J. W. Shim, *Adv. Funct. Mater.*, 2019, **29**, 1–11.
9 M. F. Müller, M. Freunek and L. M. Reindl, *IEEE J. Photovolt.*, 2013, **3**, 59–64.
10 R. Sharma, H. Lee, K. Borse, V. Gupta, A. G. Joshi, S. Yoo and D. Gupta, *Org. Electron.*, 2017, **43**, 207–213.
11 Y. S. Kim, B. K. Yu, D. Y. Kim and W. B. Kim, *Sol. Energy Mater. Sol. Cells*, 2011, **95**, 2874–2879.
12 S. H. Liao, H. J. Jhuo, P. N. Yeh, Y. S. Cheng, Y. L. Li, Y. H. Lee, S. Sharma and S. A. Chen, *Sci. Rep.*, 2014, **4**, 4–10.
13 A. Gadisa, Y. Liu, E. T. Samulski and R. Lopez, *Appl. Phys. Lett.*, 2012, **100**, 253903.
14 Y. Yan, F. Cai, L. Yang, J. Li, Y. Zhang, F. Qin, C. Xiong, Y. Zhou, D. G. Lidzey and T. Wang, *Adv. Mater.*, 2017, **29**, 1604044.
15 D. Zhang, W. C. H. Choy, F. Xie, W. E. I. Sha, X. Li, B. Ding, K. Zhang, F. Huang and Y. Cao, *Adv. Funct. Mater.*, 2013, **23**, 4255–4261.
16 S. H. Tsai, S. T. Ho, H. J. Jhuo, C. R. Ho, S. A. Chen and J. H. He, *Appl. Phys. Lett.*, 2013, **102**, 1–6.
17 V.-H. Tran, R. B. Ambade, S. B. Ambade, S.-H. Lee and I.-H. Lee, *ACS Appl. Mater. Interfaces*, 2017, **9**, 1645–1653.
18 T. Yang, M. Wang, C. Duan, X. Hu, L. Huang, J. Peng, F. Huang and X. Gong, *Energy Environ. Sci.*, 2012, **5**, 8208–8214.
19 V.-H. Tran, S. H. Eom, S. C. Yoon, S.-K. Kim and S.-H. Lee, *Org. Electron.*, 2019, **68**, 85–95.
20 G. Cheng, W. Y. Tong, K. H. Low and C. M. Che, *Sol. Energy Mater. Sol. Cells*, 2012, **103**, 164–170.
21 C. Sun, X. Li, G. Wang, P. Li, W. Zhang, T. Jiu, N. Jiang and J. Fang, *RSC Adv.*, 2014, **4**, 19529–19532.
22 C. Tozlu, A. Mutlu, M. Can, A. K. Havare, S. Demic and S. Icli, *Appl. Surf. Sci.*, 2017, **422**, 1129–1138.
23 S. K. Hau, H. L. Yip, H. Ma and A. K. Y. Jen, *Appl. Phys. Lett.*, 2008, **93**, 111–114.
24 C. H. Hsieh, Y. J. Cheng, P. J. Li, C. H. Chen, M. Dubosc, R. M. Liang and C. S. Hsu, *J. Am. Chem. Soc.*, 2010, **132**, 4887–4893.
25 K. Davis, R. Yarbrough, M. Froeschle, J. White and H. Rathnayake, *RSC Adv.*, 2019, **9**, 14638–14648.
26 H. Y. Park, D. Lim, K. D. Kim and S. Y. Jang, *J. Mater. Chem. A*, 2013, **1**, 6327–6334.
27 P. Jongnavakit, P. Amornpitoksuk, S. Suwanboon and T. Ratana, *Thin Solid Films*, 2012, **520**, 5561–5567.
28 C. Pacholski, A. Kornowski and H. Weller, *Angew. Chem., Int. Ed.*, 2002, **41**, 1188–1191.

29 H. C. Cha, Y. C. Huang, F. H. Hsu, C. M. Chuang, D. H. Lu, C. W. Chou, C. Y. Chen and C. S. Tsao, *Sol. Energy Mater. Sol. Cells*, 2014, **130**, 191–198.
30 T. Hu, P. Jiang, L. Chen, K. Yuan, H. Yang and Y. Chen, *Org. Electron.*, 2016, **37**, 35–41.
31 T. Hu, L. Li, S. Xiao, K. Yuan, H. Yang, L. Chen and Y. Chen, *Org. Electron.*, 2016, **38**, 350–356.
32 H. K. H. Lee, Z. Li, J. R. Durrant and W. C. Tsoi, *Appl. Phys. Lett.*, 2016, **108**, 253301.
33 H. Wang, C. Xie, W. Zhang, S. Cai, Z. Yang and Y. Gui, *J. Hazard. Mater.*, 2007, **141**, 645–652.
34 B. J. Richardson, X. Wang, A. Almutairi and Q. Yu, *J. Mater. Chem. A*, 2015, **3**, 5563–5571.
35 S. R. Cowan, A. Roy and A. J. Heeger, *Phys. Rev. B: Condens. Matter Mater. Phys.*, 2010, **82**, 1–10.
36 Z. Liu and N. Wang, *Adv. Opt. Mater.*, 2019, **7**, 1–11.
37 Z. Gao, L. Guo, Y. Sun, W. Qu, T. Yang, B. Li, J. Li and L. Duan, *Org. Electron.*, 2019, **67**, 232–236.
38 L. Yu, D. Luo, H. Wang, T. Zou, L. Luo, Z. Qiao, Y. Yang, J. Zhao, T. He, Z. Liu and Z. H. Lu, *Org. Electron.*, 2016, **33**, 156–163.
39 N. K. Elumalai, A. Saha, C. Vijila, R. Jose, Z. Jie and S. Ramakrishna, *Phys. Chem. Chem. Phys.*, 2013, **15**, 6831–6841.
40 N. K. Elumalai, C. Vijila, R. Jose, K. Zhi Ming, A. Saha and S. Ramakrishna, *Phys. Chem. Chem. Phys.*, 2013, **15**, 19057–19064.
41 H. Zang, Y. C. Hsiao and B. Hu, *Phys. Chem. Chem. Phys.*, 2014, **16**, 4971–4976.
42 M. C. Heiber, T. Okubo, S. J. Ko, B. R. Luginbuhl, N. A. Ran, M. Wang, H. Wang, M. A. Uddin, H. Y. Woo, G. C. Bazan and T. Q. Nguyen, *Energy Environ. Sci.*, 2018, **11**, 3019–3032.
43 M. Mohan and M. A. G. Namboothiry, *Mater. Res. Express*, 2018, **5**, 116203.
44 Y. C. Hsiao, H. Zang, I. Ivanov, T. Xu, L. Lu, L. Yu and B. Hu, *J. Appl. Phys.*, 2014, **115**, 154506.
45 D. S. Chung, H. Kong, W. M. Yun, H. Cha, H. K. Shim, Y. H. Kim and C. E. Park, *Org. Electron.*, 2010, **11**, 899–904.
46 G. Garcia-Belmonte, A. Guerrero and J. Bisquert, *J. Phys. Chem. Lett.*, 2013, **4**, 877–886.
47 C. Mondal, M. Ganguly, A. K. Sinha, J. Pal and T. Pal, *RSC Adv.*, 2013, **3**, 5937.

